Strain rate and temperature dependent viscoplasticity of sintered Cu nanoparticles

Du, Leiming; Schaffar, Gerald; Poelma, René H.; Fan, Jiajie; van Driel, Willem D.; Fan, Xuejun; Kiener, Daniel; Zhang, Guoqi; Maier-Kiener, Verena

DOI
10.1016/j.matdes.2025.114319

Publication date
2025

Document Version
Final published version

Published in
Materials and Design

Materials & Design 256 (2025) 114319

Contents lists available at ScienceDirect

Materials & Design

journal homepage: www.elsevier.com/locate/matdes

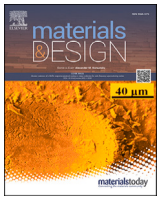

Strain rate and temperature dependent viscoplasticity of sintered Cu nanoparticles

Leiming Du [a], Gerald Schaffar [b], René H. Poelma [a], Jiajie Fan [c,*], Willem D. van Driel [a], Xuejun Fan [d], Daniel Kiener [b], Guoqi Zhang [a], Verena Maier-Kiener [b,*]

[a] Department of Microelectronics, Delft University of Technology, Mekelweg 4, Delft, 2628 CD, the Netherlands
[b] Department Materials Science, Montanuniversitat Leoben, Roseggerstrasse 12, Leoben, 8700, Austria
[c] Shanghai Engineering Technology Research Center for SiC Power Device, Academy for Engineering & Technology, Fudan University, 220 Handan Rd., Shanghai, 200433, China
[d] Department of Mechanical Engineering, Lamar University, P.O. Box 10028, Beaumont, TX 77710, USA

ARTICLE INFO

Keywords:
Sintering Cu nanoparticles
Strain rate sensitivity
Thermal softening
Anand model
Phase-field fracture method

ABSTRACT

Sintered Cu nanoparticles (NPs) are promising for high-performance electronics due to their excellent thermal and electrical conductivity, as well as mechanical reliability. This study investigates the microscale mechanical behavior of sintered Cu NPs with a bimodal particle size distribution, focusing on strain rate and temperature effects. Micro-pillar compression tests were performed across strain rates of 0.0001 s^{-1} to 0.01 s^{-1} and temperatures from 25 °C to 350 °C. Results show that higher strain rates enhance yield strength through strain-rate hardening, while elevated temperatures lead to thermal softening and reduced mechanical stability. The Anand viscoplastic model accurately predicts these deformation behaviors. Microstructural analysis via scanning electron microscopy (SEM) and transmission electron microscopy (TEM) reveals localized deformation at 175 °C, with dislocations concentrated near the top surface and persistent porosity below, whereas at 350 °C, re-sintering and grain boundary diffusion create a denser microstructure. Phase-field fracture modeling further elucidates crack propagation, emphasizing the role of pore size and temperature. This combined experimental and modeling approach enhances understanding of viscoplastic deformation and fracture mechanisms in sintered Cu NPs, informing their use in interconnects, power electronics and thermal management systems.

1. Introduction

The increasing demand for high-power and high-temperature electronic applications, such as power modules based on wide-band-gap semiconductors such as SiC and GaN, requires die-attachment materials with exceptional thermal stability, mechanical reliability and cost effectiveness [1,2]. Sintered Cu nanoparticles (NPs) have emerged as a promising alternative of solder materials due to their high melting point, excellent thermal conductivity and compatibility with power electronics packaging [3]. However, extreme operating conditions, characterized by elevated temperatures and dynamic loading, significantly influence the viscoplastic behavior and mechanical integrity of these materials [4,5]. Although nanoindentation and tensile tests have revealed temperature- and strain-rate-dependent deformation characteristics of sintered Ag [6,7] and Cu [8,9] NPs, microscale investigations under compression, particularly at elevated temperatures, remain scarce. Addressing this gap is essential for a comprehensive understanding of the interplay of strain rate and temperature on the mechanical performance and failure mechanisms of sintered Cu NPs, ensuring their reliability in next-generation power electronics.

Micro-pillar compression test has emerged as a powerful technique for investigating viscoplastic properties at the microscale, particularly under varying strain-rate conditions [10–12] and high temperatures [13–16]. By isolating the effects of nanoscale microstructural features such as grain boundaries, dislocations and porosity, this method provides critical insights into strain-rate- and temperature-dependent deformation mechanisms. In bulk Cu, high-temperature micro-pillar compression tests have revealed size-dependent plasticity, where strain rate influences dislocation pile-up and recovery mechanisms [17]. However, the viscoplastic behavior of sintered Cu NPs remains largely un-

* Corresponding authors.
E-mail addresses: jiajie_fan@fudan.edu.cn (J. Fan), verena.maier-kiener@unileoben.ac.at (V. Maier-Kiener).

https://doi.org/10.1016/j.matdes.2025.114319
Received 11 March 2025; Received in revised form 8 June 2025; Accepted 27 June 2025
Available online 2 July 2025

explored, particularly regarding the interplay between strain rate, temperature and microstructure evolution, leaving critical gaps in understanding their thermomechanical reliability for high-power electronic packaging applications [9]. Moreover, previous studies on viscoplastic deformation in sintered nanoparticle (NP) systems have primarily relied on in-situ scanning electron microscopy (SEM) tensile tests [9,18,19], which consistently reveals significant tension-compression asymmetry in sintered Cu NPs. This asymmetry stems from fundamental microstructural mechanisms: under tension, inherent sintering voids/pores act as stress concentrators that accelerate void growth and intergranular fracture, reducing ductility and strength, whereas under compression, these voids partially close while hydrostatic stress suppresses cracking, enabling higher strength through grain boundary-mediated plasticity and dislocation activity [20]. While conventional tensile test provides valuable deformation insights, its stringent sample preparation requirements and limited scalability constrain broader applicability. Most critically for viscoplastic model fitting, tensile tests typically fracture before reaching substantial plastic strains [21], preventing robust characterization of full hardening/softening behavior across essential strain-rate regimes. Consequently, micro-pillar compression test offers distinct advantages for constitutive modeling: it achieves stable plastic deformation beyond 20% strain without catastrophic failure [22], enabling complete stress-strain curve acquisition for accurate parameter calibration while facilitating in situ strain-rate jump tests on individual specimens to directly quantify rate sensitivity and activation volumes with minimal artifact interference. Therefore, this study employs micro-pillar compression test to systematically investigate the viscoplastic properties of sintered Cu NPs, addressing these limitations and providing a more comprehensive understanding of their mechanical response.

Predicting local deformation and crack propagation in porous structures is challenging due to their heterogeneity and complex microstructure. Various computational methods, including Molecular Dynamics (MD) [23,24], the extended finite element method (XFEM) [25–27], Monte Carlo (MC) simulations [28], peridynamics [29,30], and phase-field fracture modeling [31–35], have been developed to study crack evolution. Among these, phase-field fracture modeling has emerged as a particularly robust and versatile approach, as it models fractures as diffuse interfaces, eliminating the need for explicit crack tracking in XFEM. While MD provides atomic-scale insights, it is computationally prohibitive for large-scale porous structures, and MC simulations lack a direct physical basis for mechanical deformation. In contrast, phase-field fracture modeling ensures a thermodynamically consistent and computationally efficient framework, making it well-suited for simulating fracture in sintered NP networks. Despite its advantages, crack propagation in sintered NPs remains highly dependent on pore distribution. Phase-field fracture modeling has been successfully applied to sintered Ag NPs [36–38], however, studies on sintered Cu NPs remain limited. Thus, a deeper understanding of their fracture behavior is essential. To address this, this study integrates phase-field fracture modeling with Gaussian random field methods to provide a more comprehensive analysis of crack propagation in sintered Cu NPs.

In this study, we examine the mechanical properties of sintered Cu NPs under varying strain rates (0.0001 s^{-1}, 0.0005 s^{-1}, 0.001 s^{-1}, 0.005 s^{-1} and 0.01 s^{-1}) and temperatures (25 °C, 175 °C, 250 °C and 350 °C) through a combination of high-temperature micro-pillar compression test. Results show that the Anand viscoplastic constitutive model captures the material's deformation response under these conditions. Detailed microstructural characterization, conducted using SEM and transmission electron microscopy (TEM), provides critical insights into grain morphology, sintered neck formation and deformation mechanisms. In addition, phase-field fracture modeling is utilized to predict crack propagation and failure modes, enabling a quantitative assessment of damage evolution.

2. Experimental and simulation method

2.1. Sintered sample preparation

To fabricate sintered Cu NPs, Cu NP paste was firstly transferred onto an Active Metal Brazing (AMB) substrate (3 mm × 3 mm, 200 μm thick) using screen printing, where a scraper spread the paste uniformly over a patterned screen (Fig. 1a). The AMB substrate consists of a silicon nitride (Si_3N_4) ceramic core bonded to Cu layers, providing mechanical stability and thermal conductivity. Next, the printed Cu paste underwent pressure-assisted sintering at 20 MPa, 250 °C for 5 minutes under a nitrogen atmosphere using a Boschman Sinterstar system. Simultaneous application of heat and external pressure enhanced the densification of the Cu NPs, promoting strong neck formation between particles (Fig. 1b). After sintering, the aluminum (Al) film used to facilitate uniform pressure distribution was carefully removed, leaving a well-adhered, consolidated Cu layer on the substrate. The sintered Cu layer was then sectioned to isolate specific regions for mechanical characterization (Fig. 1c).

In this study, Cu NPs were synthesized via physical vapor deposition (PVD) [39]. Prior to mixing with organic compounds, the Cu NPs underwent pretreatment involving acid washing with a formic acid solution, followed by centrifugation and drying, which effectively suppressed oxidation. Subsequently, two distinct Cu particle sizes were mixed with organic compounds. SEM analysis (Fig. 1d) revealed an average particle size of 100 nm for the smaller Cu NPs and 2.5 μm for the larger particles.

The sintered Cu layer was sectioned to isolate specific regions for microstructural and mechanical characterization. As shown in Fig. 1e, SEM imaging revealed the porous structure of the as-sintered Cu NPs. A TEM sample was subsequently prepared via focused ion beam (FIB) milling using an FEI Helios G4 CX dual-beam FIB-SEM system, which highlighted the heterogeneous microstructure, including well-formed sintered necks between particles (Fig. 1f). Porosity quantification was performed using 3D FIB-SEM reconstruction, yielding a measured porosity of 7% (Fig. 1g). For mechanical test, micro-pillars with a diameter of 6 μm and a height of 20 μm (aspect ratio 3:1) were fabricated via FIB (Figs. 1h, i). This geometry ensured mechanical stability during in-situ compression tests [40].

2.2. Micro-pillar compression tests

High-temperature micro-pillar compression tests were conducted using an in-situ high-temperature SEM (HT-SEM) nanoindenter (KLA Corporation, Milpitas, CA, USA) as shown in Fig. 2a, equipped with a continuous stiffness measurement (CSM) unit [41]. The CSM system applied a 100 Hz sinusoidal force signal with a 2 nm displacement amplitude, enabling continuous determination of hardness and Young's modulus as a function of indentation depth [42]. A flat punch tip made of boron carbide (Synton-MDP, Nidau, Switzerland) was employed for precise load application. The sample is firmly clamped onto a resistance-heated sample holder (Fig. 2b), with the thermocouple positioned within a spacer. In this study, a flat-ended indenter with a 10 μm diameter, larger than the micro-pillars (Fig. 2c), was used to ensure uniform stress distribution during loading, enabling accurate assessment of the mechanical response of the sintered Cu NPs. The nanoindenter was integrated within a Tescan Vega3 SEM (Tescan, Brno, Czech Republic) under high vacuum conditions ($<10^{-4}$ mbar) to ensure accurate indent positioning and prevent high-temperature oxidation of both the tip and sample. Tip temperature calibration was performed via direct indentation into a thermocouple, following the method described by Wheeler and Michler [43]. Prior to the test, a thermal stabilization period of 1–2 hours was maintained to minimize thermal drift and ensure data reliability. The area function and frame stiffness were calibrated at room temperature using fused quartz, following the procedure outlined by Oliver and Pharr [44].

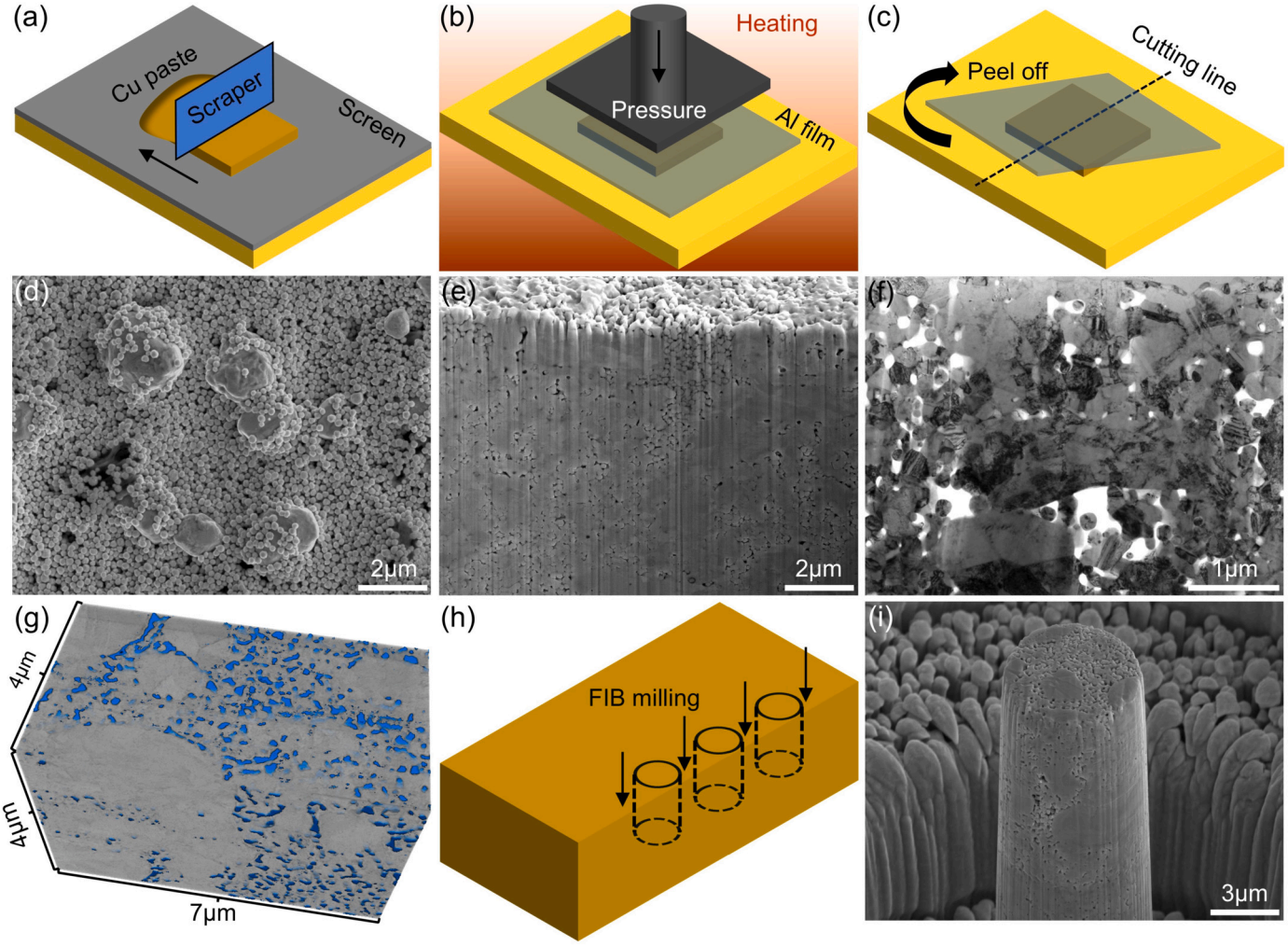

Fig. 1. Fabrication and characterization of sintered Cu NPs: (a) Screen printing of Cu NP paste onto an AMB substrate; (b) pressure-assisted sintering process under heating with an Al film cover; (c) removal of the Al film post-sintering; (d) SEM image of as-printed Cu NPs; (e) cross-sectional SEM image of sintered Cu NPs; (f) TEM image of the sintered Cu NPs; (g) 3D reconstruction of the sintered structure showing porosity; (h) schematic of FIB milling for micro-pillar fabrication; (i) SEM image of a fabricated Cu micro-pillar.

In this study, micro-pillar compression tests under varying strain rates (0.0001 s^{-1}, 0.0005 s^{-1}, 0.001 s^{-1}, 0.005 s^{-1} and 0.01 s^{-1}) and temperatures (25 °C, 175 °C, 250 °C and 350 °C) were performed. To ensure experimental reproducibility and statistical robustness, five micro-pillars were tested for each condition. Post-compression analyses involved field emission scanning electron microscopy (FE-SEM, Helios G4Cx) to examine failure modes of micro-pillars. Additionally, TEM (Cs-corrected Titan) characterization was performed to provide detailed insights into microstructure evolution and deformation mechanisms, such as dislocation activity and grain boundary interactions at elevated temperatures.

2.3. Anand constitutive model

To quantify the strain-rate and temperature-dependent behavior of the sintered Cu NPs, the Anand model is employed to fit the stress-strain data. The Anand model is a viscoplastic constitutive model widely used to describe the deformation behavior of materials, particularly under varying strain rates and temperatures [45]. The model assumes that the inelastic strain rate is related to the stress through a set of material-specific constants, which account for time-dependent plasticity and temperature effects.

$$\tilde{\sigma} = cs \tag{1}$$

here $c = g(T, \dot{\epsilon}_p)$ and $s = h(T, \dot{\epsilon}_p)$ represent the material parameter and the internal variable, respectively. Both are functions of the absolute temperature and the inelastic strain rate. Under a constant strain rate, the specific expressions for these parameters are as follows:

$$c = \frac{1}{\xi}\sinh^{-1}\left(\left(\frac{\dot{\epsilon}_p}{A}\exp\left(\frac{Q}{RT}\right)\right)^m\right), \quad c < 1 \tag{2}$$

where ξ represents the multiplier of stress, $\dot{\epsilon}_p$ denotes the inelastic strain rate, A is the pre-exponential factor, Q is the activation energy, R refers to the universal gas constant, T is the absolute temperature and m indicates the strain rate sensitivity.

Mathematically, the Anand model can also be expressed as follows,

$$\dot{\epsilon}_p = A\exp\left(-\frac{Q}{RT}\right)\left[\sinh\left(\frac{\xi\tilde{\sigma}}{s}\right)\right]^{\frac{1}{m}} \tag{3}$$

and the internal variable s was proposed by Anand [46] and Brown et al. [45] as follows:

$$\dot{s} = \left[h_0\left(1 - \frac{s}{s^*}\right)^a \operatorname{sign}\left(1 - \frac{s}{s^*}\right)\right]\dot{\epsilon}_p, \quad a \geq 1 \tag{4}$$

$$s^* = \hat{s}\left(\frac{\dot{\epsilon}_p}{A}\exp\left(\frac{Q}{RT}\right)\right)^n \tag{5}$$

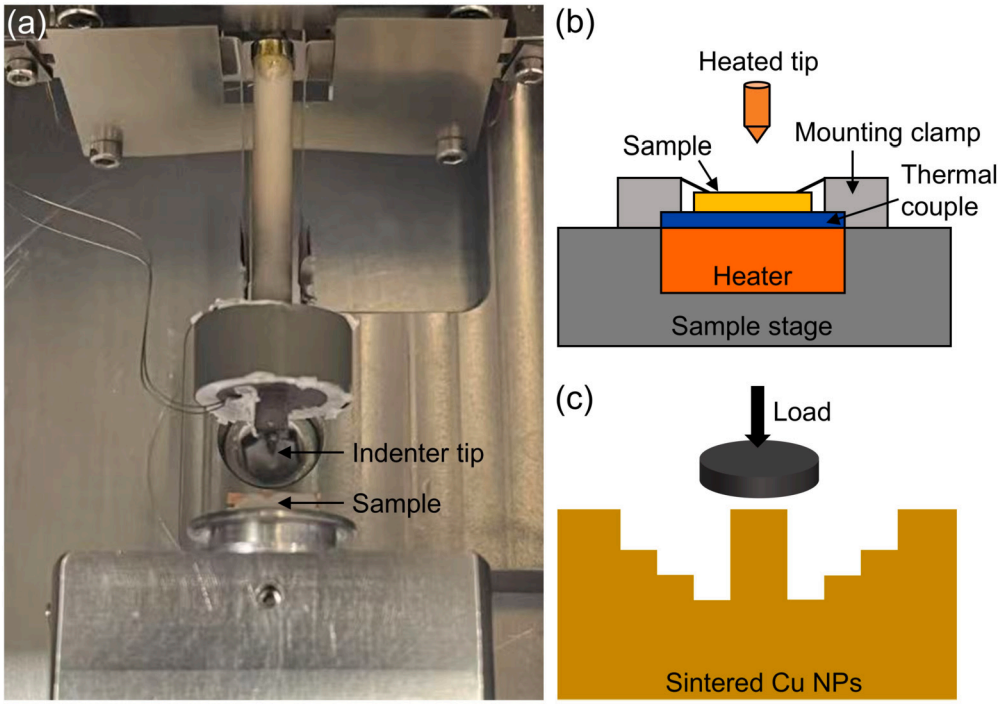

Fig. 2. (a) HT-SEM setup with nanoindenter; (b) schematic of the heating stage with sample mounting; (c) schematic of the micro-pillar compression test.

where s^* represents a saturation value of s associated with a set of given temperature and strain rates, h_0 is the hardening/softening constant, a is the strain rate sensitivity of hardening/softening, $\hat{s}$ and n are the coefficient and strain rate sensitivity of the saturation value of deformation resistance, respectively.

To determine the above parameters, Eq. (4) can be written as:

$$\dot{s} = h(\sigma, s, T)\dot{\epsilon}_p \tag{6}$$

where h is dynamic hardening and recovery function. Combining Eqs. (1) and (6) can lead to the following formula:

$$\frac{d\tilde{\sigma}}{d\epsilon_p} = ch \tag{7}$$

For the case $s < s^*$, Eqs. (4), (6) and (7) will lead to

$$\frac{d\tilde{\sigma}}{d\epsilon_p} = ch_0\left(1 - \frac{\tilde{\sigma}}{\tilde{\sigma}^*}\right)^a \tag{8}$$

where $\sigma^* = cs^*$ is the saturation or steady state stress. The integration form of Eq. (8) is

$$\tilde{\sigma} = \tilde{\sigma}^* - \left\{(\tilde{\sigma}^* - \tilde{\sigma}_0) + (a-1)\left[ch_0(\tilde{\sigma}^*)^{-a}\dot{\epsilon}_p\right]^{\frac{1}{1-a}}\right\} \tag{9}$$

where $\tilde{\sigma}_0 = cs_0$. s_0, the initial deformation resistance, representing the initial value of s. For $a = 1$, Eq. (8) can be integrated as shown below:

$$\tilde{\sigma} = \tilde{\sigma}^* - (\tilde{\sigma}^* - \tilde{\sigma}_0)\exp\left\{-\left(\frac{ch_0}{\tilde{\sigma}^*}\right)\dot{\epsilon}^p\right\} \tag{10}$$

In the compression test, $\tilde{\sigma} = |\sigma|$, where σ is the compressive stress measured in the compression experiments. Moreover, when the plastic flow is fully developed at a certain temperature T and strain rate $\dot{\epsilon}$, it can be assumed that $\dot{\epsilon}^p \approx [\dot{\epsilon}]$. Since a constant true strain rate is considered in this manuscript, the combination of Eqs. (3) and (5) can be expressed as follows:

$$\sigma^* = \frac{\hat{s}}{\xi}\left(\frac{z}{A}\right)^n \sinh^{-1}\left[\left(\frac{z}{A}\right)^m\right] \tag{11}$$

where

$$z = \dot{\epsilon}\exp\left(\frac{Q}{RT}\right) \tag{12}$$

Therefore, nine parameters (s_0, Q, A, ξ, m, h_0, a, $\hat{s}$, and n) are required in the Anand model. Steps of fitting the nine parameters are as follows [45]:

1. Determining the saturation stress σ^* for each test based on the steady-state value of the stress-strain data.
2. Determining a, ch_0 and $\tilde{\sigma}$ by fitting Eq. (9) or (10) using the least squares method.
3. Determining A, Q, m, n and the combined term $\xi/\tilde{s}$ by fitting Eq. (11) using least squares method.
4. Determining ξ by substituting the above parameter values into Eq. (2) and ensuring that c is less than 1 for each test. Then, $\hat{s}$ can be calculated from ξ and $\xi/\tilde{s}$.
5. Determining h_0 by using the following equation:

$$h_0 = \frac{\sum_{i=1}^{n}\frac{(ch_0)_i}{c_i}}{n} \tag{13}$$

where i refers to the i-th test, n represents the total number of tests. Finally, s_0 is determined from σ_0 and c obtained from each test.

2.4. Generation of random porous structures

The microstructures of sintered Cu NPs are characterized by random variations in pore geometry, including size, shape and spatial distribution, which arise from particle migration, deformation and coalescence during the sintering process. To effectively capture these characteristics, a Gaussian Random Field (GRF)-based approach was employed to generate two-dimensional (2D) microstructures [37,38,47–49]. This method models spatial randomness through a random field $Z(x)$ characterized by a mean function $m(x)$ and a covariance function $C(x_1, x_2)$. The mean function was set to zero ($m(x) = 0$) to preserve spatial neutrality, while the covariance function controlled the spatial correlation and was expressed as:

$$C(x_1, x_2) = \sigma^2\exp\left(-\frac{(x_1 - x_2)^2}{\lambda_x^2} - \frac{(y_1 - y_2)^2}{\lambda_y^2}\right) \tag{14}$$

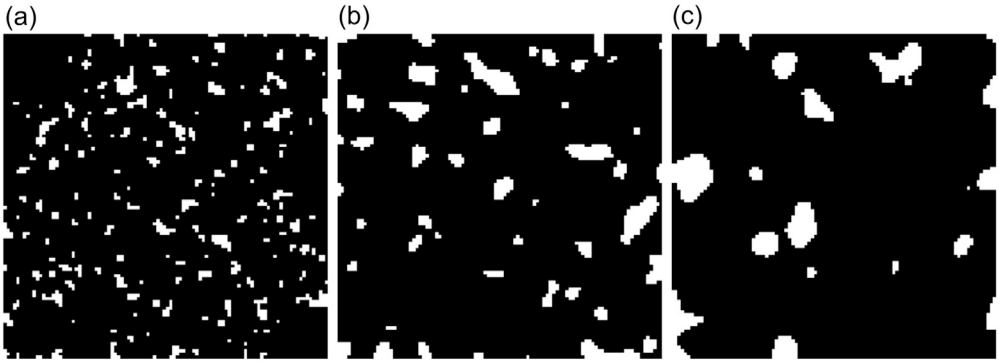

Fig. 3. 2D random porous structures: (a) $\lambda_x = \lambda_y = 2$; (b) $\lambda_x = \lambda_y = 4$; (c) $\lambda_x = \lambda_y = 6$.

where σ^2 represents the variance, and λ_x and λ_y are the correlation lengths in the x- and y-directions, respectively. By adjusting λ_x and λ_y, both isotropic and anisotropic structures can be generated, enabling control over pore aspect ratios and orientations [37,38,49]. This flexibility allows the method to simulate flattened pore shapes typically observed under directional pressure or temperature gradients.

To discretize the GRF into solid and pore phases, a threshold function was employed. The indicator function, defined as:

$$\Psi(x) = \begin{cases} 1, & Z(x) \geq F_0, \\ 0, & Z(x) < F_0. \end{cases} \tag{15}$$

This threshold (F_0) was optimized using quantile functions to ensure the target porosity level was met. The Gaussian width (σ) controlled the smoothing of the field, influencing the connectivity and size of the pores. Larger values of σ resulted in larger, less numerous pores, whereas smaller values generated finer, denser pore distributions.

The computational domain, a 2D grid of size 100×100, was constructed, and Gaussian filtering was applied to generate the random fields. The spatial correlations in the generated microstructures were validated by comparing statistical features, including pore size distributions, aspect ratios, and shape factors, to experimental results obtained from SEM imaging. By varying λ_x and λ_y, pores size and distribution aligned with the observed experimental morphology were reproduced. Therefore, the 2D models established in this study have the porosity of 7%. Fig. 3 shows the 2D random porous structure and different λ_x and λ_y, in which the black area represent the Cu domain and the white area represent the voids.

2.5. Phase-field fracture model

The phase-field fracture method, based on Griffith's fracture theory [50], regularizes cracks using a diffusive scalar damage variable $\phi \in [0, 1]$. Here, $\phi = 0$ represents undamaged material, $\phi = 1$ indicates complete fracture, and intermediate values ($0 < \phi < 1$) describe the transition zone [51]. The damage zone width is controlled by the phase-field length scale parameter l. This approach formulates fracture as a minimization problem of the total potential energy functional. For the AT1 model [52], the total potential energy is expressed as:

$$\Pi = \int_{\Omega} \left[(1-\phi)^2 + k\right] \psi_0(\boldsymbol{\epsilon}(\mathbf{u}))\, \mathrm{d}\Omega + \int_{\Omega} G_c \gamma(\phi, \nabla\phi)\, \mathrm{d}\Omega \tag{16}$$

where $\Psi(\mathbf{u}, \phi) = [(1-\phi)^2 + \mathrm{k}]\Psi_0(\epsilon)$ is the degradation function associated with the AT1 and AT2 models, $\psi_0(\epsilon) = \frac{1}{2}\epsilon^T \mathbf{C}_0 \epsilon$ is the internal strain energy under the conditions of small deformations with $\epsilon = \frac{1}{2}\left(\nabla\mathbf{u} + \nabla^T\mathbf{u}\right)$, $\mathbf{u}$ is the displacement and G_c is the critical energy release rate. As depicted in Fig. 4, this equation is provided in a 2D arbitrary solid domain Ω with a discontinuous boundary Γ.

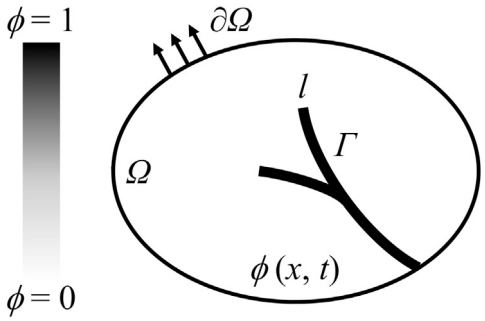

Fig. 4. Illustration of a solid body with a distinct internal discontinuity, using the phase field method to approximate the discontinuity.

The crack surface area density function is expressed as [53]:

$$\gamma(\phi; \nabla\phi) = \frac{\phi^2}{2l} + \frac{l}{2}|\nabla\phi|^2 \tag{17}$$

Within this framework, crack growth can be predicted along any trajectory without arbitrary criteria, driven by global energy minimization and the conversion of stored energy into fracture energy. The displacement and phase fields are obtained by minimizing the functional, where the functional derivatives with respect to each field are set to zero. This process yields the strong form of the problem, expressed through the following Euler–Lagrange equations [51]:

$$\frac{\delta\Pi}{\delta\mathbf{u}} = \nabla \cdot \boldsymbol{\sigma} = 0, \tag{18}$$

$$\frac{\delta\Pi}{\delta\phi} = G_c\left(\frac{\phi}{l} - l\nabla^2\phi\right) - 2(1-\phi)\psi_0(\boldsymbol{\epsilon}) = 0 \tag{19}$$

To prevent crack nucleation under compressive loading, the strain energy in the intact body is partitioned into active (ψ_0^+) and inactive (ψ_0^-) components. This decomposition distinguishes tensile and compressive contributions, addressing the tension–compression symmetry inherent in damage evolution within the phase-field framework. Such symmetry can lead to unphysical crack growth under compressive stress states, which contradicts the observed resistance to cracking in materials like metals. There are several methods for strain energy decomposition designed to prevent crack growth under compressive loading. These include the volumetric–deviatoric split proposed by Amor et al. [54], the spectral decomposition introduced by Miehe and co-workers [53], and the purely tensile splits, often referred to as no-tension models, developed by Freddi and Royer-Carfagni [55,56] and Lo et al. [57]. This study employs a volumetric–deviatoric split of the strain tensor, coupling only the deviatoric component with phase-field evolution, ensuring that compressive energy does not drive crack propagation [54]. The split strain energy contributions (ψ_0^+, ψ_0^-) are functions of their respective strain tensors, as shown below:

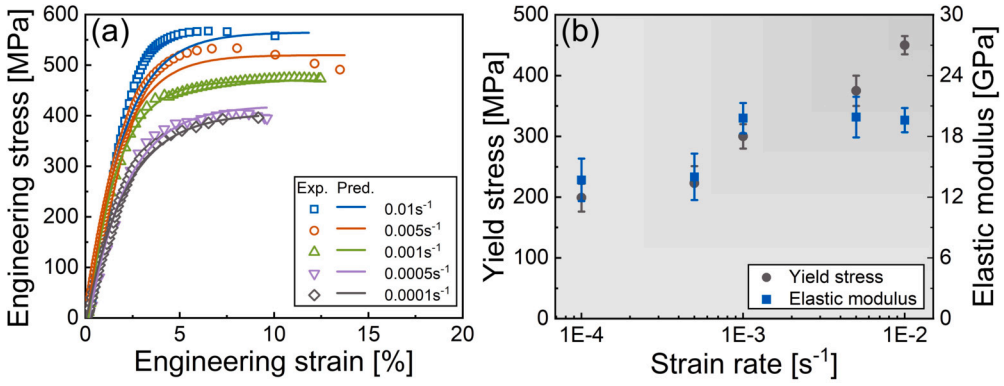

Fig. 5. (a) Stress-strain curves versus strain rates; (b) elastic modulus and yield stress versus strain rates.

$$\psi_0^+ = \frac{1}{2}\lambda\langle \mathrm{tr}(\varepsilon^+)\rangle^2 + \mu \mathrm{tr}\left[(\varepsilon^+)^2\right] \tag{20}$$

$$\psi_0^- = \frac{1}{2}\lambda\langle \mathrm{tr}(\varepsilon^-)\rangle^2 + \mu \mathrm{tr}\left[(\varepsilon^-)^2\right] \tag{21}$$

where λ and μ are the Lamé constant, ε^+ and ε^- are the positive and negative counterparts of the strain tensor.

Moreover, to prevent damage from self-healing over time τ, H (fracture driving force) is introduced as a history variable since it is an irreversible process [53].

$$H = max_{t\in[0,t]}\Psi^+(t) \tag{22}$$

This expression represents the peak tensile elastic energy attained during the loading history, serving as the primary driving force for crack propagation. This leads to the following formulation of the strong form:

$$G_c\left(\frac{\phi}{l_0} - l_0\nabla^2\phi\right) - 2(1-\phi)H = 0 \tag{23}$$

The model is implemented in the implicit finite element solver Abaqus using a user-defined material subroutine (UMAT). To simplify the analysis, the phase-field parameter is represented as a temperature-like field by utilizing coupled temperature–displacement elements. This formulation exploits the mathematical analogy between the phase-field governing equations and the steady-state heat transfer equation (Eq. (24)), as described in [58], where k is the thermal conductivity, T is temperature and r is the heat source term.

$$k\nabla^2 T = -r \tag{24}$$

$$\nabla^2\phi = \frac{\phi}{l^2} - 2(1-\phi)\frac{H}{f(\alpha)G_c l} \tag{25}$$

Specifically, the UMAT developed by Navidtehrani et al. [58–60] is employed, which incorporates both the heat transfer law and phase-field equations. Taking k as 1, a heat source is introduced in the model through the user-defined heat generation subroutine as:

$$r = -\left(\frac{\phi}{l^2} - 2(1-\phi)\frac{H}{f(\alpha)G_c l}\right) \tag{26}$$

This approach ensures computational efficiency and enables seamless integration within the Abaqus framework [61]. By representing the phase field through the temperature field, it leverages Abaqus's built-in features to effectively simulate fracture.

3. Results and discussion

3.1. Stress-strain curves under different strain rates

The stress-strain curves of micro-pillars tested under five different strain rates (0.0001 s^{-1} to 0.01 s^{-1}) are shown in Fig. 5a. The results demonstrate a clear strain-rate-hardening characteristics in the mechanical properties of sintered Cu NPs. The yield strength was determined according to 0.2% offset yield criterion [62]. As the strain rate increases, both yield stress and ultimate strength rise significantly. For instance, the yield stress exceeds 450 MPa at 0.01 s^{-1}, while it falls below 200 MPa at 0.0001 s^{-1}. This trend indicates that higher strain rates enhance resistance to deformation due to limited time for dislocation motion and rearrangement, leading to dislocation accumulation and increased strength. Conversely, lower strain rates provide more time for dislocations to rearrange, reducing yield stress but improving ductility. Fig. 5b further reveals that the elastic modulus also increases with strain rate, rising from approximately 14 GPa at 0.0001 s^{-1} to nearly 20 GPa at 0.01 s^{-1}. The observed step-like increase in elastic modulus near a strain rate of 0.001 s^{-1} can be attributed to rate-dependent deformation mechanisms in the sintered Cu NP structure. At lower strain rates, localized deformation at inter-particle necks and void growth dominate, resulting in reduced stiffness due to heterogeneous stress distribution. In contrast, higher strain rates enhance interparticle load transfer and suppress localized damage, promoting more uniform stress fields and effective cohesion across the structure. This transition leads to a measurable increase in apparent stiffness. Similar behavior has been reported in prior studies [63], where high strain rates were shown to induce more homogeneous deformation through concurrent activation of both favorable and less favorable sites. These findings highlight the role of strain rate in strengthening and stiffening sintered Cu NPs through microstructure confinement and stress redistribution.

3.2. Stress-strain curves under different temperatures

The mechanical behavior of sintered Cu NPs under compression is strongly influenced by temperature, as shown in Fig. 6. Stress-strain curves in Figs. 6a and c demonstrate significant mechanical degradation with increasing temperature (25 °C to 350 °C) at strain rates of 0.001 s^{-1} and 0.01 s^{-1}. At room temperature, micro-pillars exhibit the highest yield strength and elastic modulus, exceeding 300 MPa and 20 GPa, respectively. However, both properties decline sharply at elevated temperatures. For instance, the yield stress drops to approximately 110 MPa at 175 °C and further reduces to below 50 MPa at 350 °C, accompanied by a corresponding decrease in elastic modulus to less than 2 GPa. This temperature-induced softening is attributed to thermally activated processes such as enhanced dislocation motion [64], grain boundary sliding and atomic diffusion [65,66], which collectively reduce structural integrity. At lower temperatures, deformation resistance is dominated by dislocation pile-ups and particle necking, preserving mechanical strength. However, as temperature increases, diffusion-assisted grain boundary migration promotes plastic flow and weakening the material. Similar behavior has been observed in other nanostructured materials [13], where high-temperature deformation is linked to grain boundary effects and interfacial weakening. Additionally, strain-rate hardening effects mitigate softening to some extent. As shown in Figs. 4b and d, higher strain rates (0.01 s^{-1}) result in consistently higher yield stress and elastic modulus compared to lower rates (0.001 s^{-1})

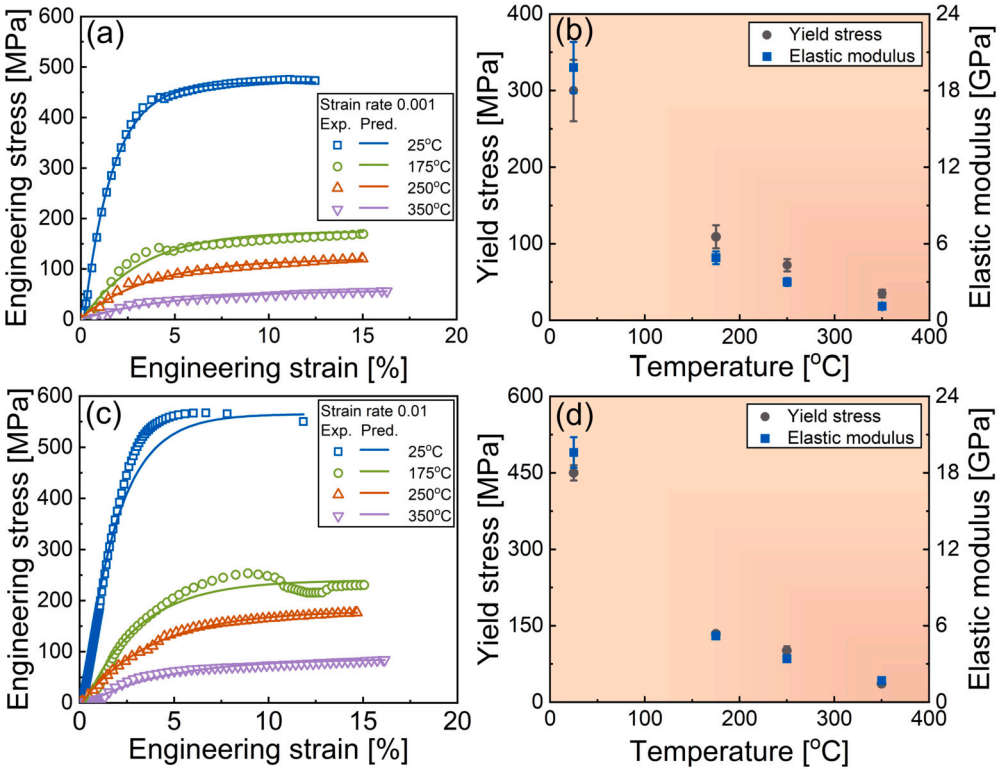

Fig. 6. Stress-strain curves versus temperature at the strain rate of (a) 0.001 s^{-1} and (c) 0.01 s^{-1}; elastic modulus and yield stress versus temperature at the strain rate of (b) 0.001 s^{-1} and (d) 0.01 s^{-1}.

Table 1
Material parameters of Anand model for the sintered Cu NPs.

Parameter	A (s^{-1})	Q (J/mol)	m	n	ξ	$\hat{s}$ (MPa)	h_0 (MPa)	s_0 (MPa)	a
Value	298	71013	0.477	0.0179	10	421	213	12.22	1

across all temperatures. This rate-dependent strengthening arises from restricted dislocation motion and reduced time for diffusion, limiting void growth and enhancing load transfer within the sintered structure. The overall trend highlights the challenges of using sintered Cu NPs in high-temperature applications, where thermal degradation of mechanical properties may lead to premature failure under elevated thermal and mechanical loads.

The material parameters of Anand model for the sintered Cu NPs are presented in Table 1. It can be observed from Fig. 5a and Figs. 6a, c that the Anand model provides a good fit to the experimental data, as indicated by the close alignment between the scatter points (experimental data) and the lines (fitted results). The fitting is particularly accurate at lower temperatures and for higher strain rates, where the plastic behavior of the material dominates. However, some discrepancies can be noticed at higher temperatures, especially in the early stages of deformation, where the model slightly underestimates the yield point. This may be due to the fact that the Anand model is primarily designed to capture plastic deformation and is less effective in modeling the initial elastic response. Despite these minor deviations, the model demonstrates a robust capability to predict the overall stress-strain behavior across different strain rates and temperatures, making it a reliable tool for predicting the mechanical response of sintered Cu NPs under varying conditions.

3.3. SEM analysis

The SEM micrographs in Fig. 7 and Fig. 8 reveal the deformation mechanisms of sintered Cu NP micro-pillars under varying strain rates and temperatures. Figs. 7a and b show micro-pillars deformed at 25 °C under strain rates of 0.0001 s^{-1} and 0.01 s^{-1}, respectively. Despite the differences in strain rate (Fig. 5a), both SEM micrographs (Figs. 7a and b) exhibit similar macroscopic deformation features, characterized by surface extrusions on the sidewalls of the compressed micro-pillars. These extrusions indicate localized plastic deformation, which likely originates from particle rearrangement and interfacial sliding—a common mechanism in sintered NP systems [67–69]. Given the absence of visible slip bands, twinning, or grain boundary migration at this resolution, the deformation is inferred to be dominated by interfacial plasticity and densification through pore collapse rather than crystallographic slip. The role of larger particles as load-bearing elements is also evident, suggesting heterogeneous stress distribution and localized deformation pathways within the pillar. Thus, the observed behavior reflects the unique mechanical response of porous sintered structures, where deformation is governed more by interparticle dynamics than by traditional intragranular mechanisms [70].

Figs. 8a–f provide high-resolution SEM micrographs of sintered Cu NP micro-pillars compressed at elevated temperatures of 175 °C and 350 °C. At both temperatures, distinct thermally activated deformation mechanisms are observed. Notably, surface extrusions and lateral shear steps (Figs. 8b, c, e, and f) suggest the onset of localized shear deformation, likely facilitated by reduced yield strength and increased particle mobility. These features are indicative of surface flow and interfacial sliding due to the fine-grained, porous microstructure of the sintered NP pillars. The reduction in visible porosity, especially at 350 °C (Figs. 8d–f), supports a densification mechanism akin to pressure-

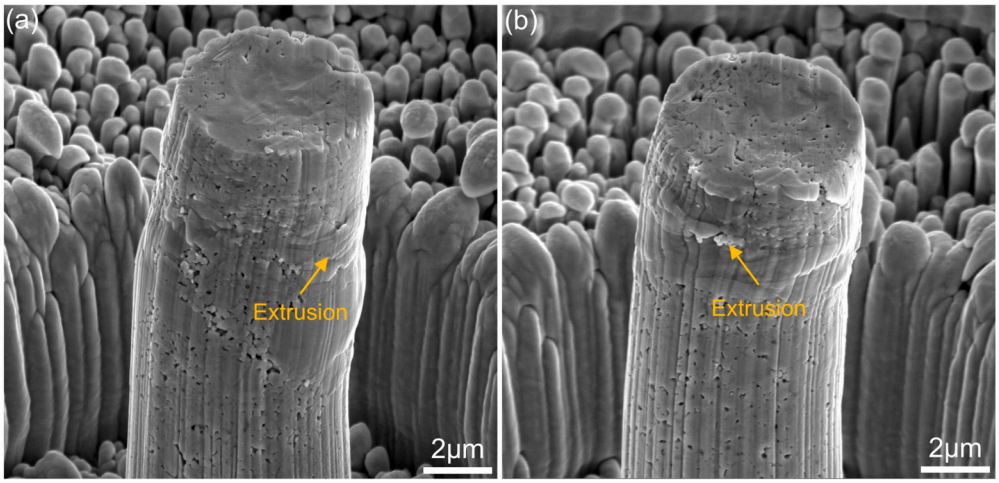

Fig. 7. Typical morphologies of micro-pillars compressed at (a) 0.001 s^{-1} and (b) 0.01 s^{-1}.

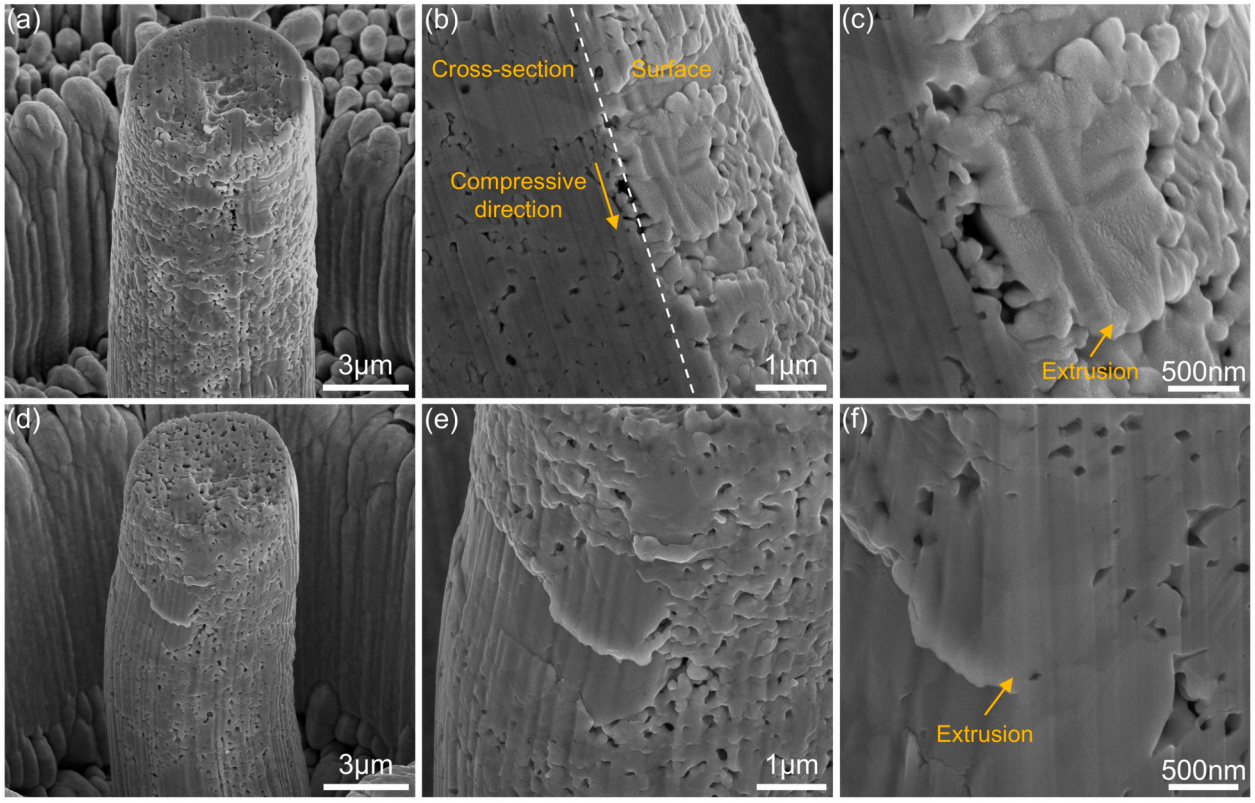

Fig. 8. SEM images of micro-pillars compressed at a strain rate of 0.001 s^{-1}. (a–c) Deformation behavior at 175 °C: (a) overall pillar morphology; (b, c) high-magnification views highlighting shear banding and surface extrusion features. (d–f) Deformation behavior at 350 °C: (d) overall pillar morphology; (e, f) high-magnification views showing enhanced shear and extrusion deformation.

assisted sintering, where elevated temperature enhances atomic diffusion and facilitates void closure [71]. This is further supported by smoother surface morphologies and fewer discrete interparticle voids. The contrast between deformation at room temperature (Fig. 7) and elevated temperatures (Fig. 8) underscores a transition in dominant mechanisms: from rigid-body particle interactions and force chain formation at 25 °C to thermally activated interparticle sliding, shear localization, and pore collapse at 175 °C and 350 °C. These observations suggest that deformation at elevated temperatures is governed by a combination of viscous flow, interface sliding and diffusion-assisted particle rearrangement [72].

3.4. TEM characterization

To further investigate the effect of high temperature on microstructure evolution of micro-pillars, two TEM samples were extracted from the compressed micro-pillars tested at 175 °C and 350 °C (Fig. S1), respectively. Fig. 9 presents TEM bright-field (BF) images of a micro-pillar compressed at 175 °C, highlighting the effect of moderate thermal activation on microstructure evolution as the re-sintering were found based on the more sphere voids compared with the initial microstructure shown in Fig. 1f. As shown in Fig. 9a, the overall morphology retains clear particle boundaries and exhibits a heterogeneous structure with

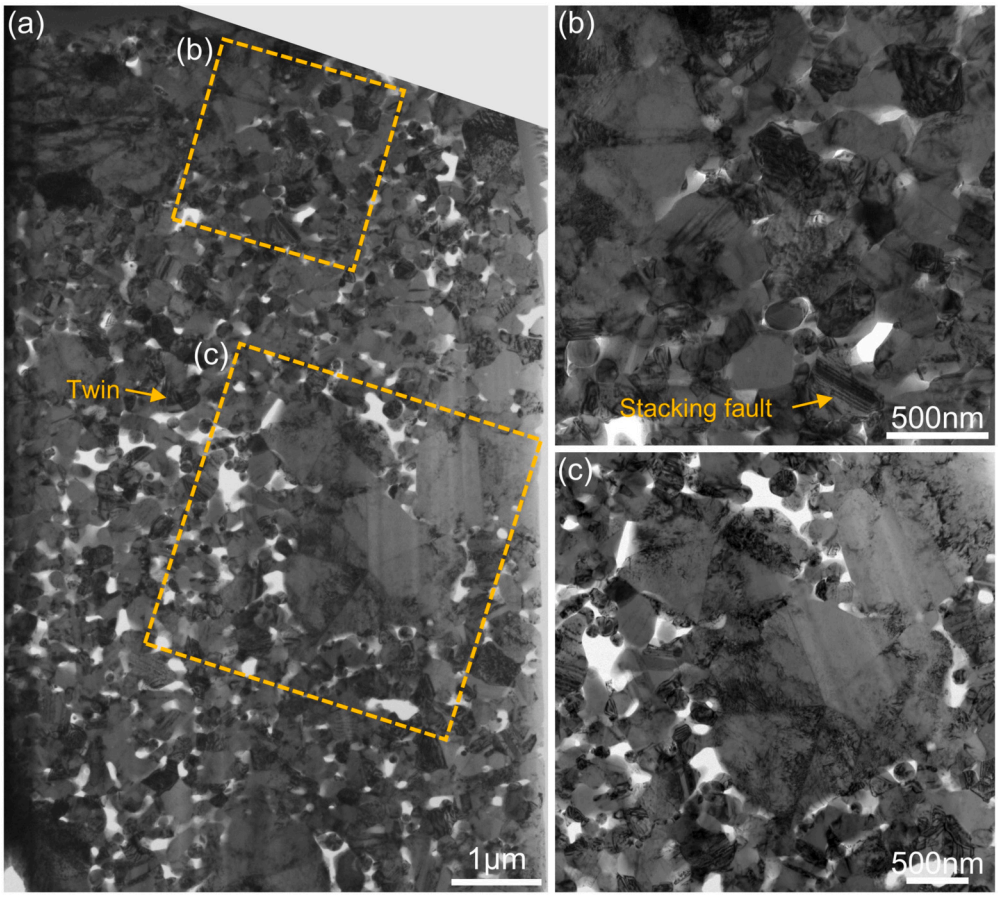

Fig. 9. TEM images of a sintered Cu NP micro-pillar compressed at 175 °C to 15% strain (strain rate: 0.001 s^{-1}). (a) Low-magnification overview of the deformed pillar; (b, c) high-magnification views of the regions indicated in (a), highlighting local microstructural features.

regions of localized deformation. Near the top surface (Fig. 9b), where the indenter applied load, deformation is more concentrated due to localized stress, promoting dislocation motion and compaction, especially within larger particles. These larger particles serve as primary load carriers, forming force chains that sustain deformation and redistribute stress. In contrast, the lower region (Fig. 9c) shows less deformation, with more evident voids and distinct particle boundaries, indicative of incomplete densification. While partial re-sintering has occurred, as evidenced by reduced porosity compared to room-temperature samples, the residual voids within the NP regions suggest that densification at 175 °C is not yet sufficient to form a fully compact structure. Instead, the deformation is predominantly accommodated through particle rearrangement and localized sliding, with plasticity concentrated at particle necks rather than across the entire structure. This highlights the critical role of particle size and arrangement in governing deformation behavior under moderate thermal conditions.

Fig. 10 illustrates microstructure changes in a micro-pillar compressed at 350 °C, where higher thermal activation significantly enhances densification through re-sintering. Due to the re-sintering, the voids present a more sphere shape compared with the initial microstructure (Fig. 1f). The BF images (Figs. 10a, b) show that the micro-pillar develops a more compact and homogeneous structure, with pronounced reductions in void size and clearer evidence of particle bonding. This densification is driven by increased dislocation activity, grain boundary sliding and diffusion-assisted particle rearrangement at elevated temperatures. The stronger sintering necks between particles further improve mechanical integrity, enabling more uniform stress distribution throughout the structure. Notably, the scanning transmission electron microscopy (STEM) image in Fig. 10c provides additional insights into the microstructure. It reveals finer voids distributed along grain boundaries, indicating that re-sintering processes are concentrated at particle interfaces, further reducing porosity. The blurred particle boundaries observed in Fig. 10c suggest enhanced bonding due to thermal diffusion, which promotes better stress transfer between particles. Compared to the sample deformed at 175 °C, the micro-pillar compressed at 350 °C exhibits not only higher compaction but also a more homogeneous deformation pattern throughout the entire volume (Fig. 10). This transition from localized deformation in a porous network to uniform plastic flow in a denser structure highlights the increasing influence of temperature-activated mechanisms. In particular, signs of dynamic recrystallization (DRX) can be inferred from the microstructural evolution observed in the high-temperature sample. The presence of finer, equiaxed grains and reduced dislocation density in certain regions (Fig. 10c) suggests the occurrence of DRX, likely facilitated by grain boundary migration and dislocation rearrangement [73,74]. These features are indicative of thermally activated recovery and recrystallization processes, which are known to enhance plastic deformability and structural stability under elevated temperatures. Therefore, we believe that DRX plays a significant role in accommodating strain and promoting densification during high-temperature deformation of sintered Cu NP micro-pillars.

Moreover, TEM observations reveal the presence of stacking faults and deformation twins, as shown in Fig. 9 and Fig. 10. These features are indicative of partial dislocation activity and twinning—both intragranular mechanisms that accommodate plastic strain under elevated temperatures [75,76]. Their presence suggests that, in addition to interfacial sliding and particle rearrangement, thermally activated dislocation processes contribute significantly to the overall deformation behavior. While direct grain boundary sliding is not explicitly resolved, the heterogeneous contrast and local misorientations near grain interfaces imply its potential contribution, particularly at higher temperatures where

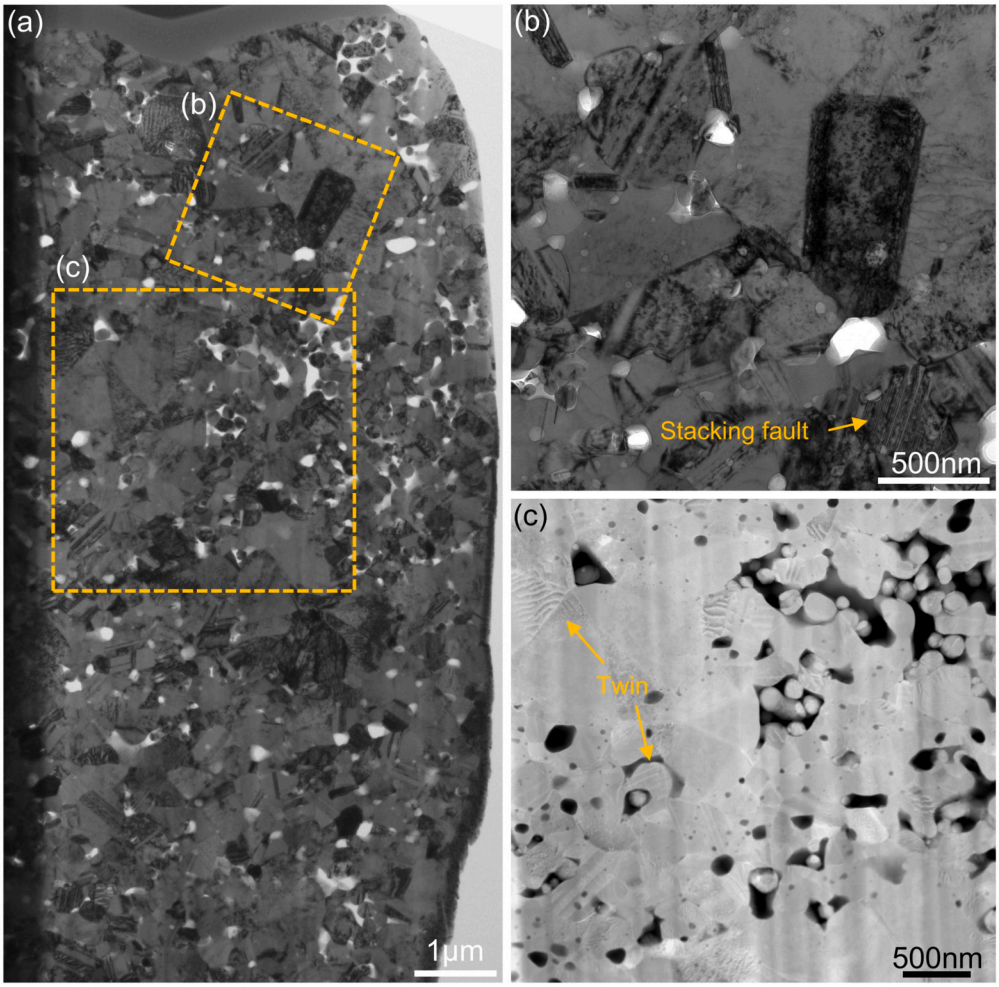

Fig. 10. TEM images of a sintered Cu NP micro-pillar compressed at 350 °C to 17% strain (strain rate: 0.001 s^{-1}). (a) Low-magnification overview of the deformed pillar; (b, c) high-magnification views of the regions indicated in (a), highlighting local microstructural features.

boundary mobility increases. Overall, these deformation products play a crucial role in enhancing the ductility and energy dissipation capacity of the sintered Cu NP micro-pillars, supporting a transition from rigid interparticle force networks at room temperature to more distributed, defect-mediated plasticity at elevated temperatures.

3.5. Phase-field fracture modeling

In this section, 2D models with randomly distributed pores are used to simulate the mechanical properties and fracture behavior. The dimension of the model is 5 μm × 5 μm with quadrilateral elements of 0.05 μm × 0.05 μm. Fig. 11 shows the corresponding finite element mesh (4 nodes CPS4) of the structure and the boundary conditions. The compressive and tensile loading is applied along the top edge (as indicated by the arrows), which is designed to simulate compressive and tensile stress, allowing for the investigation of how the porous microstructure influences mechanical behavior, particularly crack initiation and propagation.

The phase-field modeling results presented in Figs. 12-15 highlight the significant influence of void size and distribution on the mechanical behavior and crack evolution of sintered Cu NPs under compressive and tensile loading. The microstructures, controlled by the correlation lengths λ_x and λ_y, demonstrate that increasing these parameters leads to larger voids and fewer voids at a fixed porosity (7%). Stress–strain responses under compressive loading (Fig. 12) reveal that smaller voids ($\lambda_x = \lambda_y = 2$) sustain higher stress levels due to more uniform stress distributions, which delay crack initiation and promote sudden brittle-like fracture. In contrast, larger voids ($\lambda_x = \lambda_y = 4$, $\lambda_x = \lambda_y = 6$) experience localized stress concentrations at void edges and tips, causing grad-

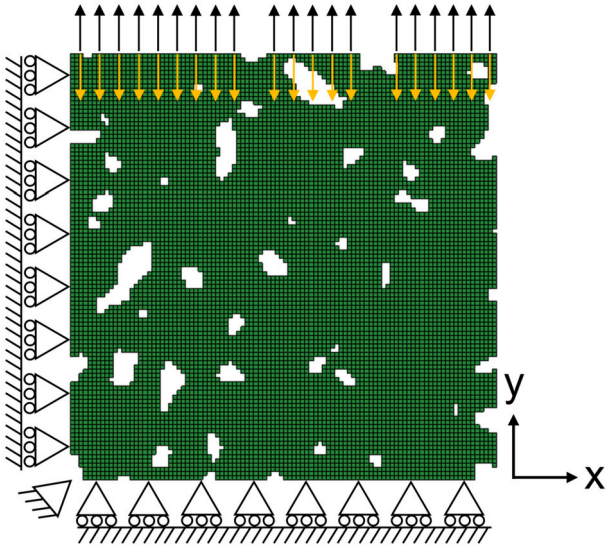

Fig. 11. Meshed 2D model with boundary conditions.

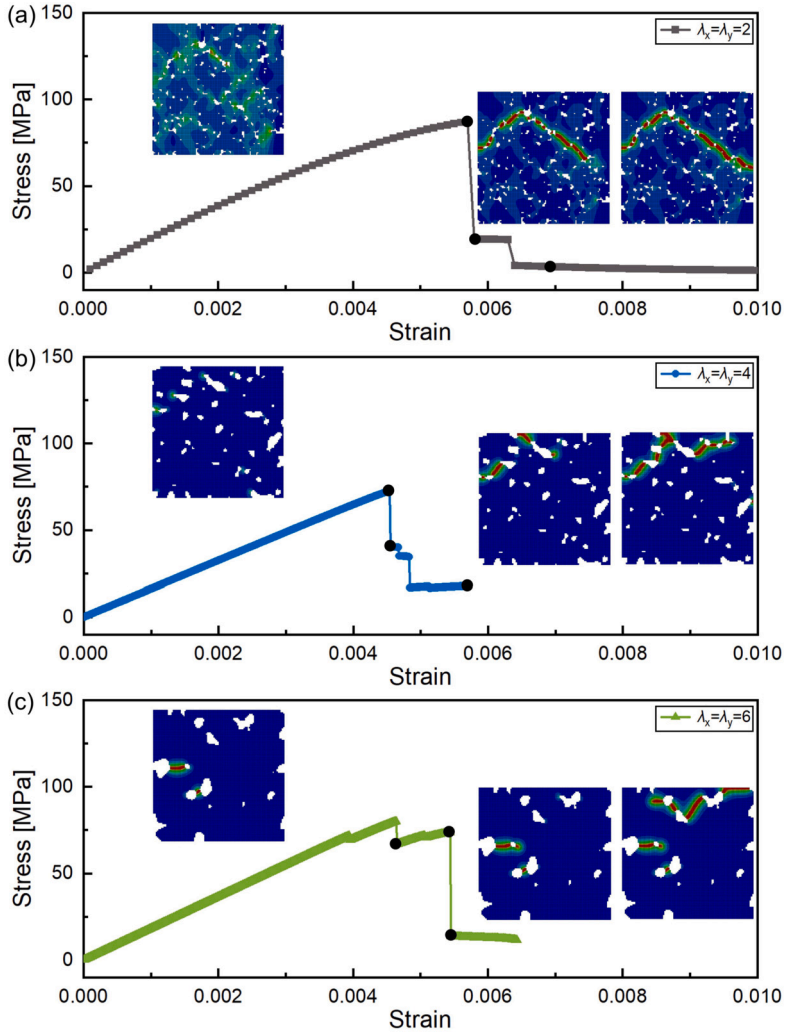

Fig. 12. Stress–strain responses with crack evolutions under compressive load: (a) $\lambda_x = \lambda_y = 2$; (b) $\lambda_x = \lambda_y = 4$; (c) $\lambda_x = \lambda_y = 6$.

ual crack propagation along interconnected voids. The stress and strain distributions (Fig. 13) further confirm that larger voids induce higher strain localization, weakening load transfer and accelerating failure. Moreover, the simulated crack propagation path agrees well with the experimental results in Fig. 8. Under tensile loading (Fig. 14), smaller voids also exhibit higher tensile strength and slower crack propagation compared to larger voids, which promote rapid crack extension along stress concentration regions. Unlike compression, tensile cracks result in complete void opening, leading to a sharp reduction in load-bearing capacity, as illustrated by the stress and strain fields in Fig. 15.

These results underscore the critical role of void morphology in governing the mechanical performance of sintered Cu NPs. Smaller voids effectively distribute stress, offering higher structural integrity and resistance to deformation, while larger voids act as stress concentrators, amplifying localized deformation and accelerating fracture propagation. The asymmetric crack evolution between compressive and tensile loading highlights distinct failure mechanisms, where compression-induced cracks are dominated by slip and void coalescence, while tensile cracks propagate through void opening [77]. The findings are consistent with experimental observations and previous studies on porous materials, demonstrating the importance of void geometry in mechanical responses and fracture paths [37]. Furthermore, the observed void evolution represents high-temperature effects, such as re-sintering and void growth, which alter stress pathways and mechanical stability. These insights provide a foundation for optimizing microstructures in sintered Cu NPs to enhance thermal and mechanical performance, particularly for high-temperature applications in electronics packaging.

Fig. 16 presents the stress–strain responses of sintered Cu NPs, demonstrating the influence of temperature (25 °C, 175 °C, 250 °C and 350 °C) on mechanical behavior and crack propagation under compressive and tensile loading. The results reveal a substantial reduction in strength with increasing temperature, primarily attributed to thermally induced softening. Notably, only the elastic modulus was adjusted in the present simulations to capture temperature-dependent effects, focusing on mechanical responses without explicitly modeling temperature-induced plasticity. While the phase-field fracture modeling effectively simulates crack initiation and propagation under various loading conditions, the real deformation mechanisms in sintered Cu NPs are inherently more complex, involving significant elastic–plastic interactions and time-dependent processes such as creep and stress relaxation. The simplified elastic modeling may underestimate the role of plastic deformation, which is critical for accurately predicting failure behavior under elevated temperatures. Future efforts should incorporate elastic–plastic formulations into the phase-field framework to better capture the interplay between plastic flow, void growth and crack evolution. Such enhancements will provide deeper insights into temperature-driven microstructural transformations and improve the predictive capabilities for applications requiring thermal and mechanical stability.

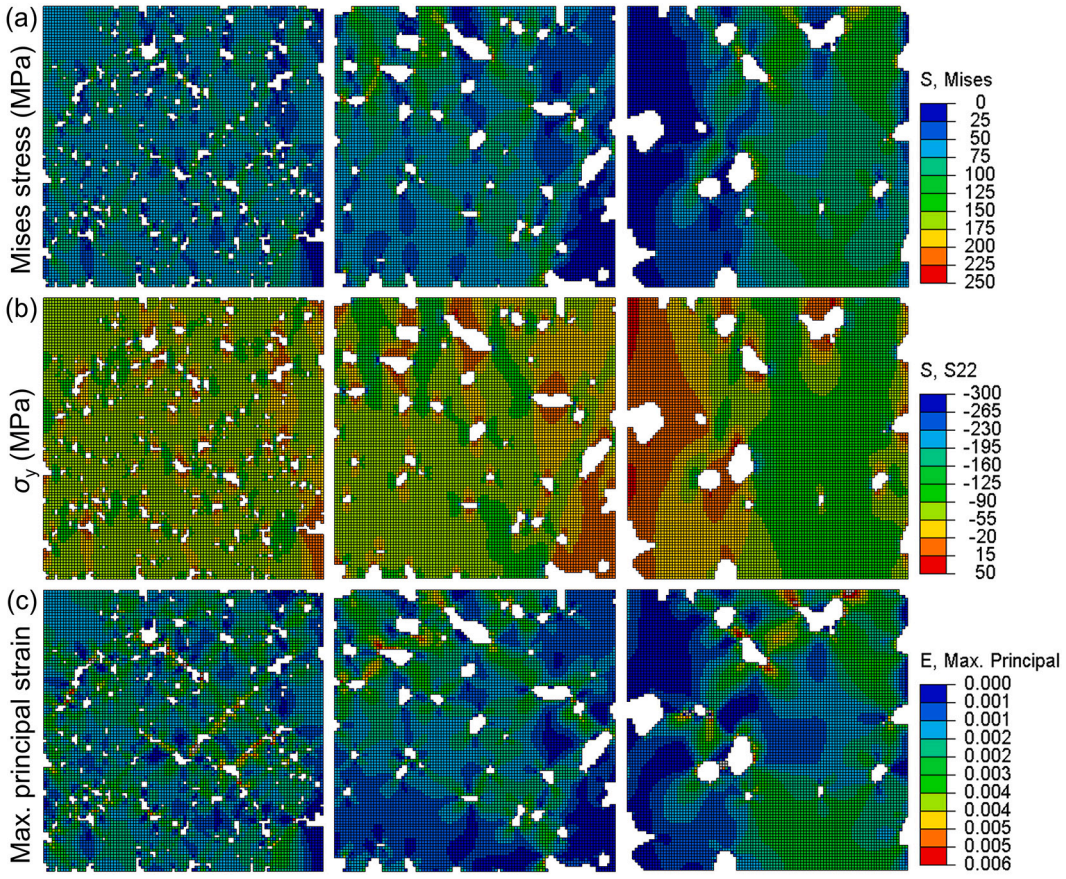

Fig. 13. The distributions of Mises stress, stress in y direction, and maximum principal strain under compressive load: (a) $\lambda_x = \lambda_y = 2$; (b) $\lambda_x = \lambda_y = 4$; (c) $\lambda_x = \lambda_y = 6$.

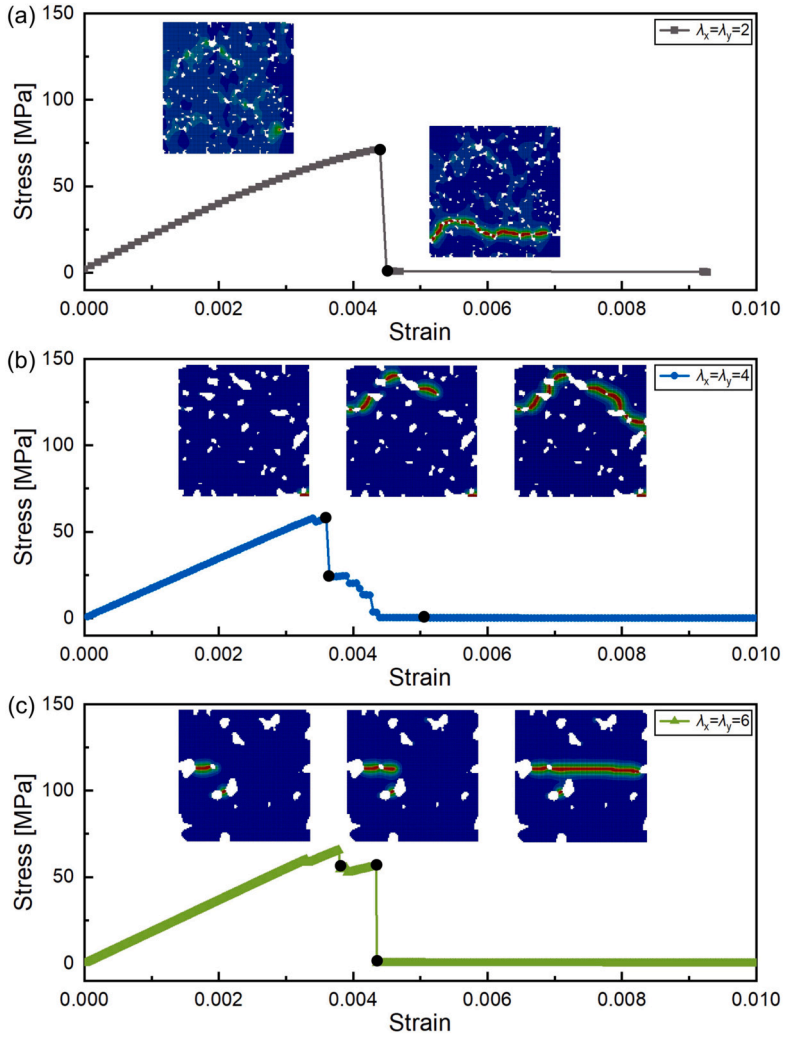

Fig. 14. Stress–strain responses with crack evolutions under tensile load: (a) $\lambda_x = \lambda_y = 2$; (b) $\lambda_x = \lambda_y = 4$; (c) $\lambda_x = \lambda_y = 6$.

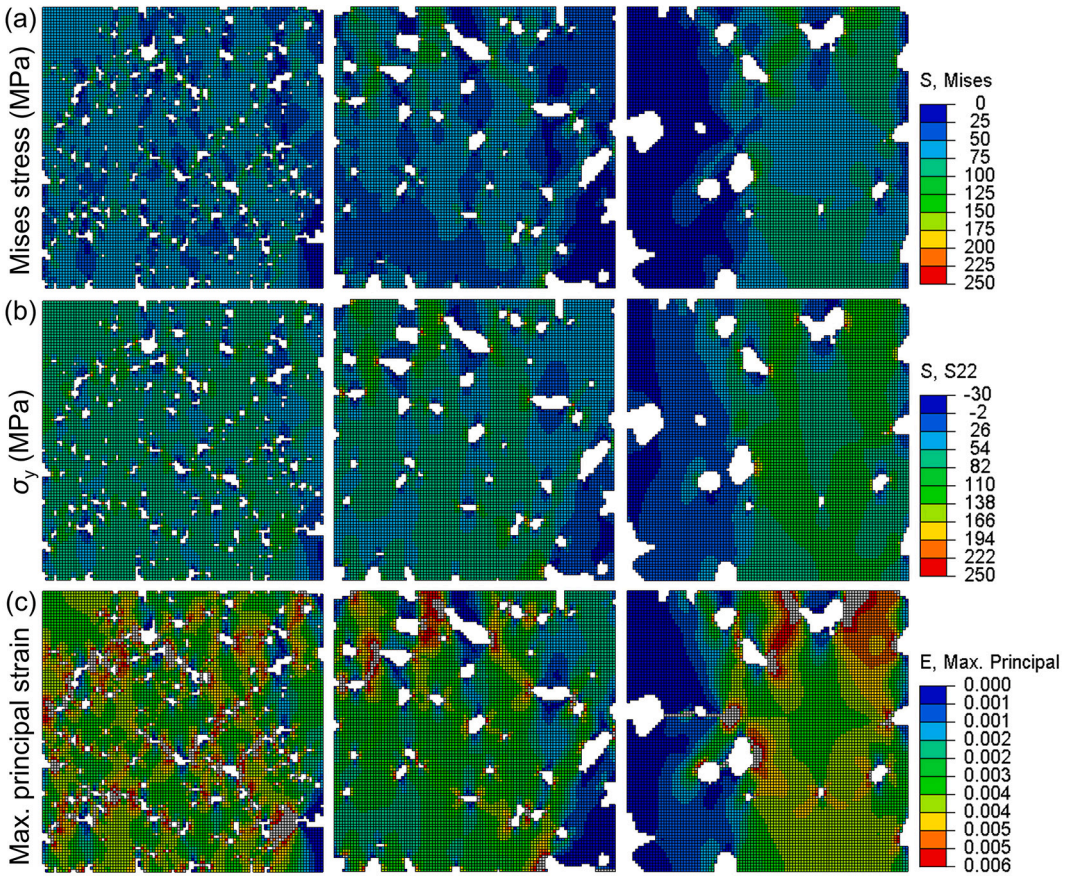

Fig. 15. The distributions of Mises stress, stress in y direction, and maximum principal strain under tensile load: (a) $\lambda_x = \lambda_y = 2$; (b) $\lambda_x = \lambda_y = 4$; (c) $\lambda_x = \lambda_y = 6$.

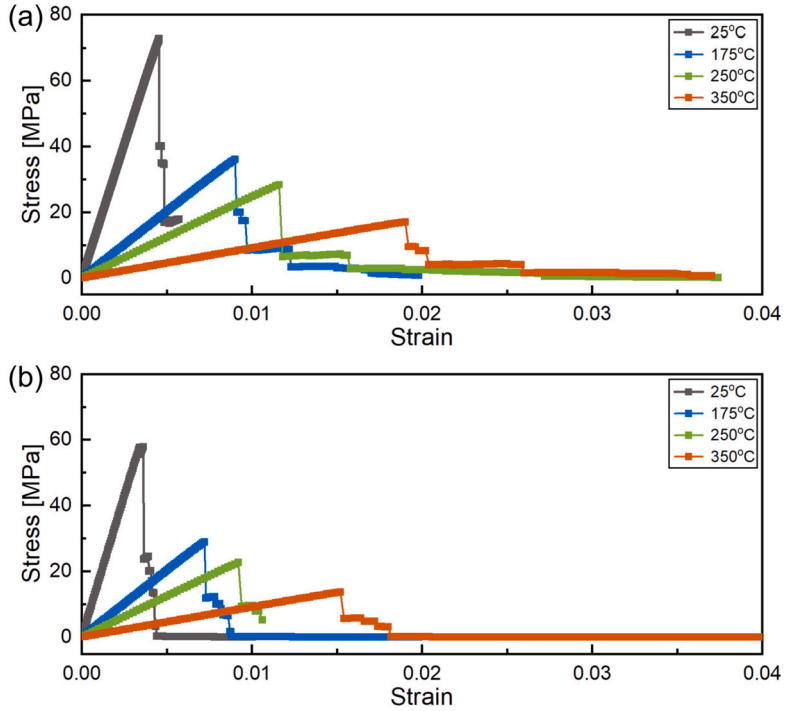

Fig. 16. Stress–strain responses of structures with different temperatures under (a) compressive load and (b) tensile load.

4. Conclusion

In this study, the microscale mechanical properties of sintered Cu NPs were comprehensively analyzed through micro-pillar compression tests, SEM, TEM and phase-field fracture modeling. This multi-faceted approach enabled a detailed exploration of the effects of strain rate and temperature on the mechanical behavior of sintered Cu NPs. The main conclusions are as follows:

1. The results reveal that the mechanical response of sintered Cu NPs is significantly influenced by strain rate and temperature. Higher strain rates enhance yield strength due to strain-rate hardening, whereas elevated temperatures induce thermal softening, leading to reduced strength and stiffness. These effects are effectively captured by the Anand viscoplastic model, which demonstrates excellent agreement with experimental stress-strain data across a range of strain rates (0.0001 s^{-1} to 0.01 s^{-1} and temperatures (25 °C to 350 °C).

2. Microstructural analyses using SEM and TEM further elucidate temperature-driven deformation mechanisms. At moderate temperatures (175 °C), deformation remains localized, with dislocation activities concentrated near particle interfaces, while at higher temperatures (350 °C), diffusion-assisted grain boundary migration promotes re-sintering and densification, resulting in a more compact structure with reduced porosity.

3. Phase-field fracture modeling reveals that void size and number significantly influence crack initiation and propagation, even at constant porosity levels. Structures with smaller, more numerous voids exhibit higher stiffness and delayed crack initiation due to more uniform stress distribution, while larger voids lead to localized stress concentrations, rapid crack coalescence and accelerated fracture propagation.

CRediT authorship contribution statement

Leiming Du: Writing – original draft, Visualization, Software, Methodology, Investigation, Conceptualization. **Gerald Schaffar:** Methodology, Investigation. **René H. Poelma:** Writing – review & editing, Supervision. **Jiajie Fan:** Writing – review & editing, Supervision. **Willem D. van Driel:** Writing – review & editing, Supervision. **Xuejun Fan:** Writing – review & editing, Supervision. **Daniel Kiener:** Writing – review & editing, Supervision. **Guoqi Zhang:** Writing – review & editing, Supervision. **Verena Maier-Kiener:** Writing – review & editing, Supervision.

Declaration of competing interest

The authors declare that they have no known competing financial interests or personal relationships that could have appeared to influence the work reported in this paper.

The author is an Editorial Board Member/Editor-in-Chief/Associate Editor/Guest Editor for *BioMedical Engineering Frontiers* and was not involved in the editorial review or the decision to publish this article.

Acknowledgements

The authors would like to acknowledge the financial support from the ECSEL Joint Undertaking (JU) under grant agreement No 876659. The JU receives support from the European Union's Horizon 2020 research and innovation program and Germany, Austria, Slovakia, Sweden, Finland, Belgium, Italy, Spain, Netherlands, Slovenia, Greece, France, and Turkey. For the Titan TEM results, we acknowledge support from the Kavli Institute of Nanoscience, Delft University of Technology, and the Netherlands Electron Microscopy Infrastructure (NEMI), project number 184.034.014, part of the National Roadmap and financed by the Dutch Research Council (NWO).

Appendix A. Supplementary material

Supplementary material related to this article can be found online at https://doi.org/10.1016/j.matdes.2025.114319.

Data availability

Data will be made available on request.

References

[1] A. Hutzler, A. Tokarski, S. Kraft, S. Zischler, A. Schletz, Increasing the lifetime of electronic packaging by higher temperatures: solders vs. silver sintering, in: 2014 IEEE 64th Electronic Components and Technology Conference (ECTC), IEEE, 2014, pp. 1700–1706.
[2] K. Sugiura, T. Iwashige, K. Tsuruta, C. Chen, S. Nagao, T. Funaki, K. Suganuma, Reliability evaluation of sic power module with sintered ag die attach and stress-relaxation structure, IEEE Trans. Compon. Packag. Manuf. Technol. 9 (4) (2019) 609–615.
[3] R. Kimura, Y. Kariya, N. Mizumura, K. Sasaki, Effect of sintering temperature on fatigue crack propagation rate of sintered ag nanoparticles, Mater. Trans. 59 (4) (2018) 612–619.
[4] G. Chen, Z.-S. Zhang, Y.-H. Mei, X. Li, D.-J. Yu, L. Wang, X. Chen, Applying viscoplastic constitutive models to predict ratcheting behavior of sintered nanosilver lap-shear joint, Mech. Mater. 72 (2014) 61–71.
[5] G. Chen, L. Yu, Y. Mei, X. Li, X. Chen, G.-Q. Lu, Uniaxial ratcheting behavior of sintered nanosilver joint for electronic packaging, Mater. Sci. Eng. A 591 (2014) 121–129.
[6] X. Long, Z. Li, X. Lu, H. Guo, C. Chang, Q. Zhang, A. Zehri, W. Ke, Y. Yao, L. Ye, et al., Mechanical behaviour of sintered silver nanoparticles reinforced by sic microparticles, Mater. Sci. Eng. A 744 (2019) 406–414.
[7] X. Long, Q. Jia, Z. Shen, M. Liu, C. Guan, Strain rate shift for constitutive behaviour of sintered silver nanoparticles under nanoindentation, Mech. Mater. 158 (2021) 103881.
[8] J. Fan, D. Jiang, H. Zhang, D. Hu, X. Liu, X. Fan, G. Zhang, High-temperature nanoindentation characterization of sintered nano-copper particles used in high power electronics packaging, Results Phys. 33 (2022) 105168.
[9] D. Hu, C. Qian, X. Liu, L. Du, Z. Sun, X. Fan, G. Zhang, J. Fan, High temperature viscoplastic deformation behavior of sintered nanocopper paste used in power electronics packaging: insights from constitutive and multi-scale modelling, J. Mater. Res. Technol. 26 (2023) 3183–3200.
[10] L. Zhao, Q. Guo, Z. Li, Z. Li, G. Fan, D.-B. Xiong, Y. Su, J. Zhang, Z. Tan, D. Zhang, Strain-rate dependent deformation mechanism of graphene-al nanolaminated composites studied using micro-pillar compression, Int. J. Plast. 105 (2018) 128–140.
[11] J. Carpenter, A. Misra, M. Uchic, P. Anderson, Strain rate sensitivity and activation volume of cu/ni metallic multilayer thin films measured via micropillar compression, Appl. Phys. Lett. 101 (5) (2012).
[12] S. Breumier, S. Sao-Joao, A. Villani, M. Lévesque, G. Kermouche, High strain rate micro-compression for crystal plasticity constitutive law parameters identification, Mater. Des. 193 (2020) 108789.
[13] S. Lotfian, M. Rodríguez, K. Yazzie, N. Chawla, J. Llorca, J.M. Molina-Aldareguía, High temperature micropillar compression of al/sic nanolaminates, Acta Mater. 61 (12) (2013) 4439–4451.
[14] O.T. Abad, J.M. Wheeler, J. Michler, A.S. Schneider, E. Arzt, Temperature-dependent size effects on the strength of ta and w micropillars, Acta Mater. 103 (2016) 483–494.
[15] J. Cho, X.L. Phuah, J. Li, Z. Shang, H. Wang, H. Charalambous, T. Tsakalakos, A.K. Mukherjee, H. Wang, X. Zhang, Temperature effect on mechanical response of flash-sintered zno by in-situ compression tests, Acta Mater. 200 (2020) 699–709.
[16] A. Abaza, J. Laurencin, A. Nakajo, M. Hubert, T. David, F. Monaco, C. Lenser, S. Meille, Fracture properties of porous yttria-stabilized zirconia under micro-compression testing, J. Eur. Ceram. Soc. 42 (4) (2022) 1656–1669.
[17] S. Yuan, Y. Zhu, S. Liang, M. Huang, Z. Li, Dislocation-density based size-dependent crystal plasticity framework accounting for climb of piled up dislocations at elevated temperature, Mech. Mater. 134 (2019) 85–97.
[18] B. Li, J. Wang, Y. Yao, Creep behavior of sintered nano-silver at high temperature: experimental and theoretical analysis, Mater. Today Commun. 37 (2023) 106956.
[19] K. Wakamoto, D. Yasugi, T. Otsuka, K. Nakahara, T. Namazu, Fracture mechanism of sintered silver film revealed by in-situ sem uniaxial tensile loading, IEEE Trans. Compon. Packag. Manuf. Technol. (2024).
[20] H.-Y. Jeong, A new yield function and a hydrostatic stress-controlled void nucleation model for porous solids with pressure-sensitive matrices, Int. J. Solids Struct. 39 (5) (2002) 1385–1403.
[21] C.C. Roth, D. Mohr, Determining the strain to fracture for simple shear for a wide range of sheet metals, Int. J. Mech. Sci. 149 (2018) 224–240.
[22] F. Bardi, S. Kyriakides, Plastic buckling of circular tubes under axial compression—part i: experiments, Int. J. Mech. Sci. 48 (8) (2006) 830–841.
[23] H. Wang, H.B. Chew, Molecular dynamics simulations of plasticity and cracking in lithiated silicon electrodes, Extrem. Mech. Lett. 9 (2016) 503–513.

[24] W. Song, Y. Yu, Y. Guan, Role of void shape on shock responses of nanoporous metallic glasses via molecular dynamics simulation, Int. J. Mech. Sci. 218 (2022) 107076.
[25] Q. Shao, L. Bouhala, A. Younes, P. Núñez, A. Makradi, S. Belouettar, An xfem model for cracked porous media: effects of fluid flow and heat transfer, Int. J. Fract. 185 (2014) 155–169.
[26] E. Mikaeili, P. Liu, Numerical modeling of shear band propagation in porous plastic dilatant materials by xfem, Theor. Appl. Fract. Mech. 95 (2018) 164–176.
[27] B.E. Hachi, A.E. Benkhechiba, M.R. Kired, D. Hachi, M. Haboussi, Some investigations on 3d homogenization of nano-composite/nano-porous materials with surface effect by fem/xfem methods combined with level-set technique, Comput. Methods Appl. Mech. Eng. 371 (2020) 113319.
[28] N. Noii, A. Khodadadian, F. Aldakheel, Probabilistic failure mechanisms via Monte Carlo simulations of complex microstructures, Comput. Methods Appl. Mech. Eng. 399 (2022) 115358.
[29] O. Karpenko, S. Oterkus, E. Oterkus, Peridynamic analysis to investigate the influence of microstructure and porosity on fatigue crack propagation in additively manufactured ti6al4v, Eng. Fract. Mech. 261 (2022) 108212.
[30] Y. Pan, P. Wu, S. Fan, X. Peng, Z. Chen, Peridynamic simulation of fatigue crack growth in porous materials, Eng. Fract. Mech. 300 (2024) 109984.
[31] C. Miehe, L.-M. Schänzel, H. Ulmer, Phase field modeling of fracture in multi-physics problems. Part I. Balance of crack surface and failure criteria for brittle crack propagation in thermo-elastic solids, Comput. Methods Appl. Mech. Eng. 294 (2015) 449–485.
[32] C. Miehe, M. Hofacker, L.-M. Schänzel, F. Aldakheel, Phase field modeling of fracture in multi-physics problems. Part II. Coupled brittle-to-ductile failure criteria and crack propagation in thermo-elastic–plastic solids, Comput. Methods Appl. Mech. Eng. 294 (2015) 486–522.
[33] E. Martínez-Pañeda, A. Golahmar, C.F. Niordson, A phase field formulation for hydrogen assisted cracking, Comput. Methods Appl. Mech. Eng. 342 (2018) 742–761.
[34] M. Dittmann, F. Aldakheel, J. Schulte, F. Schmidt, M. Krüger, P. Wriggers, C. Hesch, Phase-field modeling of porous-ductile fracture in non-linear thermo-elasto-plastic solids, Comput. Methods Appl. Mech. Eng. 361 (2020) 112730.
[35] B. He, T. Vo, P. Newell, Investigation of fracture in porous materials: a phase-field fracture study informed by reaxff, Eng. Comput. 38 (2022) 5617–5633.
[36] Y. Su, G. Fu, C. Liu, K. Zhang, L. Zhao, C. Liu, A. Liu, J. Song, Thermo-elasto-plastic phase-field modelling of mechanical behaviours of sintered nano-silver with randomly distributed micro-pores, Comput. Methods Appl. Mech. Eng. 378 (2021) 113729.
[37] Y. Su, J. Zhu, X. Long, L. Zhao, C. Chen, C. Liu, Statistical effects of pore features on mechanical properties and fracture behaviors of heterogeneous random porous materials by phase-field modeling, Int. J. Solids Struct. 264 (2023) 112098.
[38] Y. Su, Z. Shen, X. Long, C. Chen, L. Qi, X. Chao, Gaussian filtering method of evaluating the elastic/elasto-plastic properties of sintered nanocomposites with quasi-continuous volume distribution, Mater. Sci. Eng. A 872 (2023) 145001.
[39] X. Liu, S. Li, J. Fan, J. Jiang, Y. Liu, H. Ye, G. Zhang, Microstructural evolution, fracture behavior and bonding mechanisms study of copper sintering on bare dbc substrate for sic power electronics packaging, J. Mater. Res. Technol. 19 (2022) 1407–1421.
[40] A. Kurdi, S. Alshihri, T. Tabbakh, N.B. Darwish, J.B. Saedon, A.K. Basak, Compressive strength and deformation behavior of the hybrid s phase layer under micro-pillar compression, Mater. Sci. Eng. A 861 (2022) 144380.
[41] G.J. Schaffar, D. Tscharnuter, V. Maier-Kiener, Exploring the high-temperature deformation behavior of monocrystalline silicon–an advanced nanoindentation study, Mater. Des. 233 (2023) 112198.
[42] J. Kappacher, O. Renk, D. Kiener, H. Clemens, V. Maier-Kiener, How grain boundary characteristics influence plasticity close to and above the critical temperature of ultra-fine grained bcc ta2.5w, Acta Mater. 216 (2021) 117110.
[43] J. Wheeler, J. Michler, Elevated temperature, nano-mechanical testing in situ in the scanning electron microscope, Rev. Sci. Instrum. 84 (4) (2013).
[44] W.C. Oliver, G.M. Pharr, An improved technique for determining hardness and elastic modulus using load and displacement sensing indentation experiments, J. Mater. Res. 7 (6) (1992) 1564–1583.
[45] S.B. Brown, K.H. Kim, L. Anand, An internal variable constitutive model for hot working of metals, Int. J. Plast. 5 (1989) 95–130.
[46] L. Anand, Constitutive equations for the rate-dependent deformation of metals at elevated temperatures, J. Eng. Mater. Technol. 104 (1982) 12–17.
[47] M. Neumann, M. Osenberg, A. Hilger, D. Franzen, T. Turek, I. Manke, V. Schmidt, On a pluri-Gaussian model for three-phase microstructures, with applications to 3d image data of gas-diffusion electrodes, Comput. Mater. Sci. 156 (2019) 325–331.
[48] Y. Gao, Y. Jiao, Y. Liu, Ultra-efficient reconstruction of 3d microstructure and distribution of properties of random heterogeneous materials containing multiple phases, Acta Mater. 204 (2021) 116526.
[49] X. Long, J. Zhu, Y. Su, Y. Yan, C. Chang, H. Zhang, V. Salomoni, Phase field fracture modeling of mechanical degradation and crack propagation in random porous sintered nano-silver with thermal and strain-rate effects, Eng. Fract. Mech. (2024) 110753.
[50] A.A. Griffith, Vi. The phenomena of rupture and flow in solids, Philos. Trans. R. Soc. Lond., Ser. A, Contain. Pap. Math. Phys. Character 221 (582–593) (1921) 163–198.
[51] S. Waseem, C. Erdogan, T. Yalçinkaya, Phase field modeling of fatigue crack growth retardation under single cycle overloads, Int. J. Fatigue 179 (2024) 108064.
[52] B. Bahrami, H. Ahmadian, M.R. Mehraban, M.R. Ayatollahi, Mixed-mode fracture prediction of notched components using phase-field approach, Int. J. Solids Struct. 306 (2025) 113113.
[53] C. Miehe, M. Hofacker, F. Welschinger, A phase field model for rate-independent crack propagation: robust algorithmic implementation based on operator splits, Comput. Methods Appl. Mech. Eng. 199 (45–48) (2010) 2765–2778.
[54] H. Amor, J.-J. Marigo, C. Maurini, Regularized formulation of the variational brittle fracture with unilateral contact: numerical experiments, J. Mech. Phys. Solids 57 (8) (2009) 1209–1229.
[55] F. Freddi, G. Royer-Carfagni, Regularized variational theories of fracture: a unified approach, J. Mech. Phys. Solids 58 (8) (2010) 1154–1174.
[56] F. Freddi, G. Royer-Carfagni, Variational fracture mechanics to model compressive splitting of masonry-like materials, Ann. Solid Struct. Mech. 2 (2011) 57–67.
[57] Y.-S. Lo, M.J. Borden, K. Ravi-Chandar, C.M. Landis, A phase-field model for fatigue crack growth, J. Mech. Phys. Solids 132 (2019) 103684.
[58] Y. Navidtehrani, C. Betegon, E. Martinez-Paneda, A general framework for decomposing the phase field fracture driving force, particularised to a Drucker–Prager failure surface, Theor. Appl. Fract. Mech. 121 (2022) 103555.
[59] Y. Navidtehrani, C. Betegón, E. Martínez-Pañeda, A simple and robust abaqus implementation of the phase field fracture method, Appl. Eng. Sci. 6 (2021) 100050.
[60] Y. Navidtehrani, C. Betegón, E. Martínez-Pañeda, A unified abaqus implementation of the phase field fracture method using only a user material subroutine, Materials 14 (8) (2021) 1913.
[61] C.G. Dengiz, M. Dorduncu, A unified phase-field approach for failure prediction in modulus graded adhesively bonded single-lap joints, Theor. Appl. Fract. Mech. 127 (2023) 104062.
[62] J. Suryawanshi, G. Singh, S. Msolli, M.H. Jhon, U. Ramamurty, Tension-compression asymmetry and shear strength of titanium alloys, Acta Mater. 221 (2021) 117392.
[63] J. Zhao, Z. Xie, T. Zhong, T. Sun, K. Fezzaa, Y. Cai, J. Huang, S. Luo, Strain rate effects on the mechanical behavior of porous titanium with different pore sizes, Mater. Sci. Eng. A 821 (2021) 141593.
[64] A. Kodam, M. Gundi, Y. Chiu, I. Jones, S. Singh, J. Jain, A review of challenges and opportunities in micropillar compression studies in mg alloys, J. Magnesium Alloys (2023).
[65] H. Jones, V. Tong, R. Ramachandramoorthy, K. Mingard, J. Michler, M. Gee, Micropillar compression of single crystal tungsten carbide, part 1: temperature and orientation dependence of deformation behaviour, Int. J. Refract. Met. Hard Mater. 102 (2022) 105729.
[66] M. Nasim, Y. Li, C. Wen, Length-scale dependent deformation, strengthening, and ductility of fcc/fcc ni/al nanolaminates using micropillar compression testing, Acta Mater. 193 (2020) 318–328.
[67] C. Shih, M. Meyers, V. Nesterenko, High-strain-rate deformation of granular silicon carbide, Acta Mater. 46 (11) (1998) 4037–4065.
[68] M.S. Khorrami, N. Saito, Y. Miyashita, M. Kondo, Texture variations and mechanical properties of aluminum during severe plastic deformation and friction stir processing with sic nanoparticles, Mater. Sci. Eng. A 744 (2019) 349–364.
[69] Y. Ma, X. Wang, Z. Dong, P. Ni, Z. Li, H. Liu, Microstructure and mechanical performance of nickel coating on copper sheet via laser shock processing, Appl. Surf. Sci. 592 (2022) 153366.
[70] Y.T. Zhu, T.G. Langdon, Influence of grain size on deformation mechanisms: an extension to nanocrystalline materials, Mater. Sci. Eng. A 409 (1–2) (2005) 234–242.
[71] R. Chang, Q. Guo, Z. Ma, R. Ding, C. Liu, Y. Liu, Kinetics of voids evolution during diffusion bonding of dissimilar metals on consideration of the realistic surface morphology: modeling and experiments, Acta Mater. 276 (2024) 120121.
[72] R. Yuan, I.J. Beyerlein, C. Zhou, Emergence of grain-size effects in nanocrystalline metals from statistical activation of discrete dislocation sources, Acta Mater. 90 (2015) 169–181.
[73] T. Al-Samman, G. Gottstein, Dynamic recrystallization during high temperature deformation of magnesium, Mater. Sci. Eng. A 490 (1–2) (2008) 411–420.
[74] C. Cui, F. Wang, Y. Li, B. Jiao, L. Huang, W. Zhang, L. Zhou, Dynamic recrystallization and deformation model of β-quenched zr-4 alloy subjected to elevated temperature compression, Mater. Sci. Eng. A 849 (2022) 143472.
[75] R.B. Figueiredo, S. Sabbaghianrad, A. Giwa, J.R. Greer, T.G. Langdon, Evidence for exceptional low temperature ductility in polycrystalline magnesium processed by severe plastic deformation, Acta Mater. 122 (2017) 322–331.
[76] F. Yan, N. Tao, F. Archie, I. Gutiérrez-Urrutia, D. Raabe, K. Lu, Deformation mechanisms in an austenitic single-phase duplex microstructured steel with nanotwinned grains, Acta Mater. 81 (2014) 487–500.
[77] C. Chen, K. Suganuma, Microstructure and mechanical properties of sintered ag particles with flake and spherical shape from nano to micro size, Mater. Des. 162 (2019) 311–321.